Article

Nitrogen-Doped CuO@CuS Core-Shell Structure for Highly Efficient catalytic OER Application

Abu Talha Aqueel Ahmed , Abu Saad Ansari , Vijaya Gopalan Sree , Atanu Jana , Abhishek Meena , Sankar Sekar , Sangeun Cho , Hyungsang Kim , Hyunsik Im *

Posted Date: 14 November 2023

doi: 10.20944/preprints202311.0890.v1

Keywords: Water electrolysis; CuO@CuS; oxygen evolution reaction; nitrogenation; Hydrothermal growth

Article

Nitrogen-Doped CuO@CuS Core-Shell Structure for Highly Efficient Catalytic OER Application

Abu Talha Aqueel Ahmed [1], Abu Saad Ansari [2], Vijaya Gopalan Sree [1], Atanu Jana [1], Abhishek Meena [1], Sankar Sekar [1,3], Sangeun Cho [1], Hyungsang Kim [1] and Hyunsik Im [1,*]

[1] Division of Physics and Semiconductor Science, Dongguk University, Seoul 04620, Republic of Korea; talhaphy@gmail.com, sreevg@dgu.ac.kr, atanujanaic@gmail.com, pakar.abhishek@gmail.com, sangeun.c@dongguk.edu, hskim@dongguk.edu, hyunsik7@dongguk.edu

[2] Center of Excellence Applied Nanotechnology, Nano Center Indonesia Research Institute, Banten 15314, Indonesia; abusaadphy@gmail.com

[3] Quantum-Functional Semiconductor Research Center, Dongguk University-Seoul, Seoul 04620, Korea; sanssekar@gmail.com

* Correspondence: hyunsik7@dongguk.edu; Tel.: +82 2 2260 3770

Abstract: Water electrolysis is a highly efficient route to produce ideally clean H_2 fuel with excellent energy conversion efficiency and high gravimetric energy density, without producing carbon trace unlike steam methane reforming, and resolves the issues of environmental contamination via replacing the conventional fossil fuel. Of special importance lies in the advancement of highly effective non-precious catalysts for the oxygen evolution reaction (OER). The electrocatalytic activity of an active catalyst mainly depends on the material conductivity, accessible catalytically active sites, and intrinsic OER reaction kinetics, which can be tuned via introducing heteroatom N in the catalyst stricture. Herein, an efficacious nitrogenation of CuS has been accomplished, which was synthesized using hydrothermal procedure, and characterized for their electrocatalytic activity towards OER. The nitrogen-doped CuO@CuS (N,CuO@CuS) electrocatalyst exhibits superior OER activity than pristine CuS (268 and 602 mV), achieving the low overpotential of 240 and 392 mV at a current density of 10 and 100 mA/cm^2, respectively, ascribed to the favorable electronic structural modification triggered by nitrogen incorporation. The N,CuO@CuS also exhibits excellent endurance under varied current rates and a static potential response over 25 h stability measured at 10 and 100 mA/cm^2.

Keywords: water electrolysis; CuO@CuS; oxygen evolution reaction; nitrogenation; hydrothermal growth

1. Introduction

The fossil fuel technology has been a major source of energy for an eon, but it comes with significant ecological, resource, and efficiency drawbacks [1]. The dynamic change of energy needs with the rapidly developing technologies has attracted significant attention towards environmental catastrophe caused by excess use of traditional fossil fuels [2,3]. In this regard, production of renewable H_2 fuel offers a more sustainable and eco-friendlier alternative with the potential to address many of these drawbacks, especially when it is produced through the electrolysis of earth-abundant water ($2H_2O \rightarrow 2H_2 + O_2$) [4]. Water electrolysis is indeed categorized into two simultaneous half-reactions, namely: the oxygen evolution reaction (OER; $2H_2O \rightarrow 4H^+ + 4e^- + O_2$) and the hydrogen evolution reaction (HER; $2H^+ + 2e^- \rightarrow H_2$) [5]. Although, the H_2 production from water electrolysis is comparatively easy, however, O_2 production is still the bottleneck due to its sluggish reaction kinetics, which deteriorates the overall electrolyzer cell efficiency [6]. The development of energy-efficient, inexpensive, and stable OER catalysts is crucial for making water electrolysis a feasible and scalable energy conversion technology [7]. This need has inspired extensive

 doi:10.20944/preprints202311.0890.v1

research efforts to create catalyst materials composed solely of abundant and inexpensive elements [7,8].

Due to the high activity at a widespread pH range, Ru/Ir-based catalyst are still the benchmarks for OER, however, the high cost and scarcity of the precursors hinders their large-scale application [9]. In the recent years, significant interest has been devoted towards the first-row transition metal (M)-based oxyhydroxide, oxide, phosphide, chalcogenide, and carbide materials to pursue highly efficient catalysts [10,11]. Specifically, CuS-based catalysts for OER have gained considerable attention due to their cost-effectiveness, abundance supply, and excellent redox properties and therefore, have been examined as the OER catalyst for water electrolysis application [12,13]. However, the scalable application for CuS catalyst is restricted due to poor overpotential at a higher current rate and degraded performance during stability caused by sluggish OER kinetics, which is linked to the surface oxidation and corrosion of metal-sulfides in an alkaline medium [14]. These issues can be overcome by tuning the electronic structure of the active catalyst by introducing the heterogeneous N atoms through a doping process and forming a core-shell structure [15]. Generally, the M-N bonding possesses better electrical conductivity compared to the M-O and M-S bonding due to higher electronegativity of N than O and S, and the N atom possesses promising electron-withdrawing ability from adjacent Cu in the catalyst structure through a donor/acceptor interaction leading to intrinsic alterations in the electronic configurations of Cu-ions within the catalyst material [16].

Owing to the above fundamental key concept, herein, we have synthesized N-doped CuO@CuS (N,CuO@CuS) core-shell structure on the macroporous Ni foam (NF) substrate via a hydrothermal and post-nitrogenation process. The electrochemical studies reveal that introducing the heteroatom (N) enhances both electrical conductivity and catalytically active sites, which leads in turn to a higher intrinsic reaction activity of the proposed catalyst. Dramatically, in contrast to as-prepared CuS catalyst, the N,CuO@CuS core-shell catalyst exhibits exceptional characteristics in alkaline KOH medium and demonstrates reduced overpotential (240 mV), a more modest Tafel slope (138 mV dec^{-1}), and a higher turnover frequency. The N,CuO@CuS core-shell catalyst also exhibits remarkable endurance throughout the long-term stability (25 h at 10, 50, and 100 mA cm^{-2}) after insignificant change in the potential due to partial electrooxidation during initial testing in alkaline electrolyte. In addition, the N,CuO@CuS core-shell catalyst maintains the smallest voltage response compared to CuS catalyst and even with various chalcogenide-based catalysts (Figure 1a) and the obtained results were in an adequate tolerable range (Figure S1a) [11,17–22].

Preprints (www.preprints.org) | NOT PEER-REVIEWED | Posted: 14 November 2023 doi:10.20944/preprints202311.0890.v1

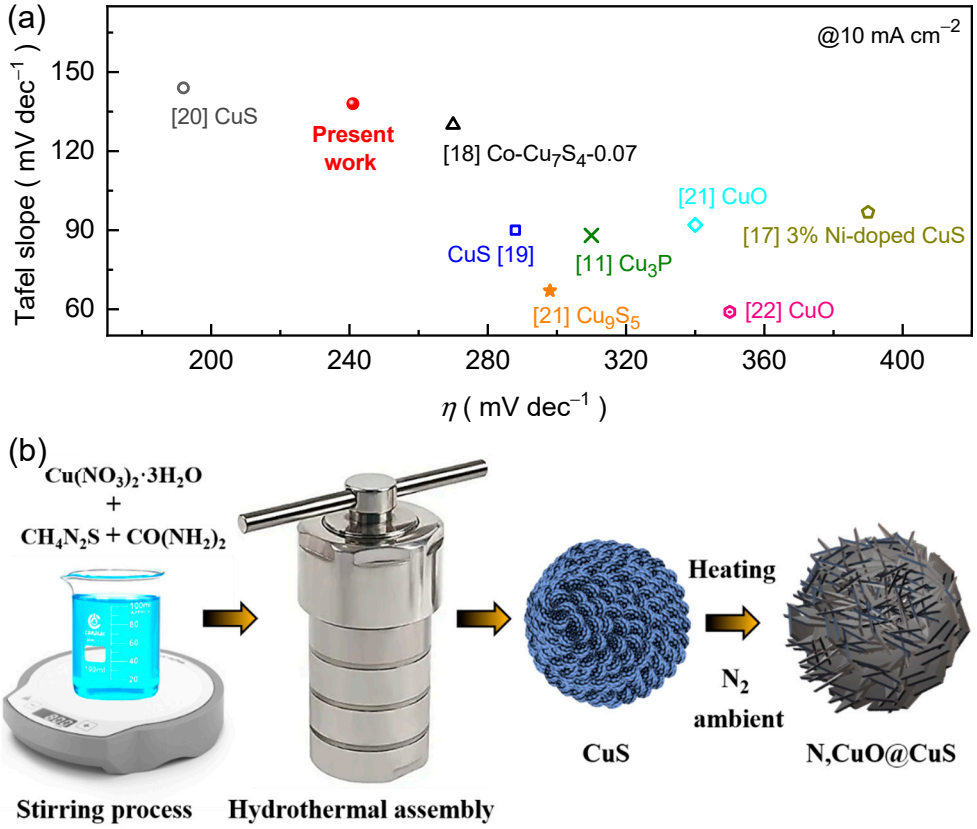

Figure 1. (a) Comparative overpotential verses Tafel plots for various Cu-based metal chalcogenide catalyst reported in 1 M KOH electrolyte medium and our N,CuO@CuS catalyst at 10 mA cm^{-2}. (b) Schematic representation of synthesis procedure for the fabrication of CuS and N,CuO@CuS catalyst.

2. Materials and Methods

2.1. Materials

All the analytical grade chemical reagents mentioned were employed in the experiment without undergoing additional purification processes. Thiourea (CH_4N_2S), copper nitrate trihydrate ($Cu(NO_3)_2{\cdot}3H_2O$), urea (CH_4N_2O), potassium hydroxide (KOH), hydrochloric acid (HCl), and ethanol (CH_3CH_2OH) were procured from Sigma Aldrich (MERCK). Macroporous three-dimensional (3D) NF substrate (used electrode size: 1 × 5 cm2) was provided by Alantum (Korea).

2.2. Synthesis of CuS and N,CuO@CuS

The CuS film was initially synthesized via a hydrothermal method and subsequently treated in a nitrogen atmosphere to obtain the desired N,CuO@CuS core-shell structure, which is shown in Figure 1b. In a typical procedure, CH_4N_2S (50 mmol) and $Cu(NO_3)_2{\cdot}3H_2O$ (5 mmol) were dissolved in water in a glass beaker containing $CO(NH_2)_2$ (30 mmol). The mixture was kept for stirring for about 30 min. at room temperature (R.T.). Thereafter, the NF (exposed area: 1 × 1 cm^2) and solution were placed in a Teflon-lined autoclave vessel. The assembly was kept into a furnace and the hydrothermal reaction proceeded for 12 h at 160 °C. After natural cooling, the deposited electrode film was takeout, washed with copious amount of deionized water and ethanol, and overnight dried in a vacuum at 80 °C. In the following step, the CuS electrode film was kept to a sealed quartz tube in a tubular furnace. After vacuuming and purging with nitrogen for an hour to remove air, the furnace was heated to 2 h at 350 °C and then cooled to R.T. The resulting N,CuO@CuS film was utilized as the catalyst electrode for the electrochemical OER test.

 doi:10.20944/preprints202311.0890.v1

2.3. Material characterization

X-ray diffraction (XRD) measurements covered a spectral angle (2θ) range of 20 to 80° at a scanning rate of 2° min.$^{-1}$, utilizing CuKα radiation (λ = 1.54056 Å). The elemental bonds and material fingerprints were examined using Raman spectra analysis using an Ar-ion laser beam (514 nm). Material morphology and composition were assessed using Field emission scanning electron microscope (FESEM) and energy dispersive spectroscopy (EDS) that were operated at 15 kV. X-ray photoelectron spectroscopy (XPS) was employed to assess the oxidation states of the constituent elements, with elemental binding energies calibrated against the chamber's contaminated carbon (C 1s at 284.33 eV). The best-fit model for all the acquired individual narrow spectra involved the utilization of Gaussian curve fitting.

2.4. Electrochemical OER testing

The electrochemical measurements for catalytic OER application were performed on an electrochemical workstation (VersaSTAT instrument). The three-electrode cell included Pt foil as the counter electrode and a saturated KCl-filled reference electrode (SCE) whereas the CuS and N,CuO@CuS films served as the working electrode, 1 M KOH was used as the electrolyte to examine all the electrochemical characteristic properties, and the potentials (V) vs. RHE were converted from V vs. SCE using this equation:

$$E_{RHE} = E°_{SCE} + (pH \times 0.059) + E_{SCE}, \quad (1)$$

where E_{SCE}, E_{RHE}, and $E°_{SCE}$ are the voltage in SCE scale, potential in RHE scale, and SCE's standard potential at R.T., respectively. The linear-scan voltammetry (LSV) curves were measured to understand the voltage response of the catalysts and the measured LSV curves were *JR*-corrected to estimate the overpotential (η) values at the driven current densities as follows:

$$\eta = E_{RHE}\ (JR\text{–corrected}) - 1.23, \quad (2)$$

$$E_{RHE}\ (JR\text{–corrected}) = E_{RHE} - (J \times Rs), \quad (3)$$

3. Results and Discussion

3.1. Morphological and Compositional Properties

The material morphology and compositions of the electrode films were assessed using FESEM and EDS image analysis. Figures 2a,b display the FESEM image of CuS and N,CuO@CuS electrode films. The CuS film (Figure 2a) reveals agglomerated compact spherical morphology with random embossed textured surface topography. The size of these spheres is in the range between 300 and 400 nm. The surface topography dramatically changed after nitrogenation (Figure 2b) and a well-defined flake-like texture appeared covering the entire CuS surface. These ultrathin nanoflakes-like embossed textured shell (i.e., CuO) on the surfaces of interconnected sphere could prevent degradation of catalytic activity of the formed material and the incorporated N atom further result in the higher specific surface area and faster electrochemical reaction kinetics. The EDS mapping image of N,CuO@CuS core-shell structure (Figure 2c) reveals the uniform distribution of Cu, S, N, and O elements. Compared to pure electrode film (Figure S2,S3), the presence of additional N and O constituents in the doped electrode film confirms the successful attachment of N atom in the CuS structure and the simultaneous surface transition during the process, which results in the core-shell structure formation after nitrogenation process.

Preprints (www.preprints.org) | NOT PEER-REVIEWED | Posted: 14 November 2023 doi:10.20944/preprints202311.0890.v1

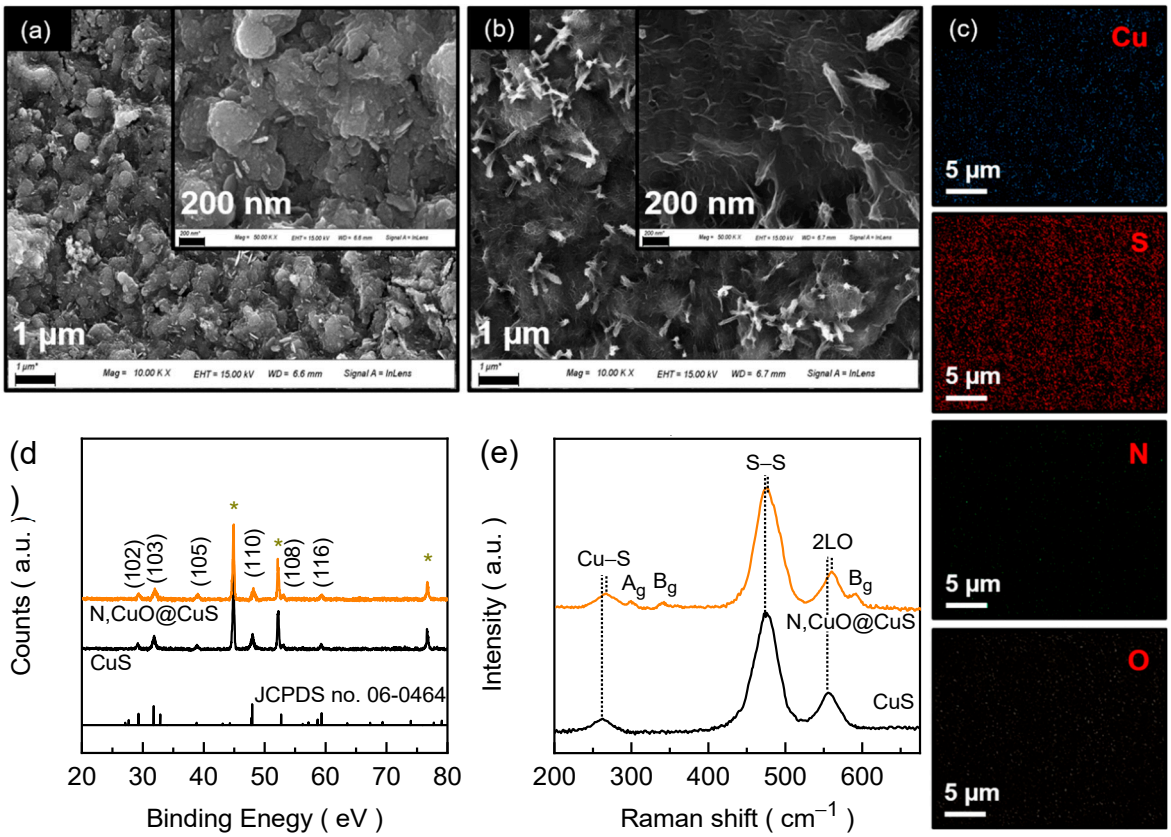

Figure 2. FESEM images of (**a**) CuS and (**b**) N,CuO@CuS core-shell structure. (**c**) EDS image mapping for N,CuO@CuS electrode film. (**d**) XRD and (**e**) Raman spectra of CuS and N,CuO@CuS core-shell structure films.

3.2. Crystallographic Characteristics

Material phase and crystallographic structure identification were determined through XRD technique. Figure 2d shows the XRD spectra for CuS and N,CuO@CuS core-shell structure catalyst electrodes along with the relevant JCPDS pattern. The CuS electrode exhibits the Bragg's diffractions at $2\theta = 29.18°$, 31.84°, 38.82°, 48.02°, 53.00°, and 59.32°, which correspond to (102), (103), (105), (110), (108), and (116) reflection planes of CuS (JCPDS card no. 06–0464), respectively. For the N,CuO@CuS core-shell structure, the XRD peaks shifted slightly towards higher diffraction angle with slightly broadened FWHM compared to pure CuS, suggesting the reduced interplanar lattice spacing of the formed core-shell structure compared to the pure CuS due to successful attachment of N atoms, which has the lower atomic radius of N (0.075 nm) than those of S (0.102 nm) and Cu (0.138 nm) [15,23]. Further, the structural bonding arrangement in the electrode materials was analyzed using Raman spectral analysis. Figure 2e shows the Raman spectra of CuS and N,CuO@CuS electrode films. The CuS electrode film demonstrates the Raman vibrational peaks at 265 cm^{-1}, 474 cm^{-1}, and 557 cm^{-1} correspond to the Cu–S vibration, S–S ions symmetric stretching at the 4e site, and phonon longitudinal overtone, respectively [14,19,24]. The Raman spectrum N,CuO@CuS core-shell structure is identical to the pure CuS with three additional humps originating from Ag (299 cm^{-1}) and Bg (342 and 591 cm^{-1}) modes of the amorphous CuO [25,26]. Besides, the Raman peaks of the core-shell structure, which are identical to CuS exhibit blue shift in the peak position due to increased vibrational frequency arising from the varied surface state of CuS upon nitrogenation.

3.3. Chemical state Characteristics

The elemental binding states of the electrode films were examined using XPS spectral analysis. Figure 3a depicts the full-range survey spectra of the CuS and N,CuO@CuS electrode films, which

Preprints (www.preprints.org) | NOT PEER-REVIEWED | Posted: 14 November 2023 doi:10.20944/preprints202311.0890.v1

reveals the presence of emission peaks of the constituent element. Figure 3b shows the well-resolved narrow Cu 2p spectra for CuS and N,CuO@CuS electrode film. The CuS electrode film demonstrates the typical XPS signals of Cu $2p_{3/2}$ (932.27 eV) and Cu $2p_{1/2}$ (952.26 eV) with a binding-energy difference of 19.99 eV (~ 20 eV), confirming the presence of Cu^{2+} state of Cu in CuS structure [27]. The remaining two peaks are associated with satellite peaks of the paramagnetic chemical state of Cu^{2+} located at 942.11 and 962.85 eV (marked as "Sat." in Figure 3b) [28]. The N,CuO@CuS electrode film also shows similar characteristic peaks in the Cu 2p emission spectra, however, the emission peak positions are slightly blue-shifted compared to that of pure CuS electrode film, suggesting that the N atom doping in the CuS structure leads to reduced electron density around the neighboring S atoms and its electrons are more tightly bound to the nucleus because of higher electronegativity and electron-trapping capability of nitrogen than sulfur atom [29].

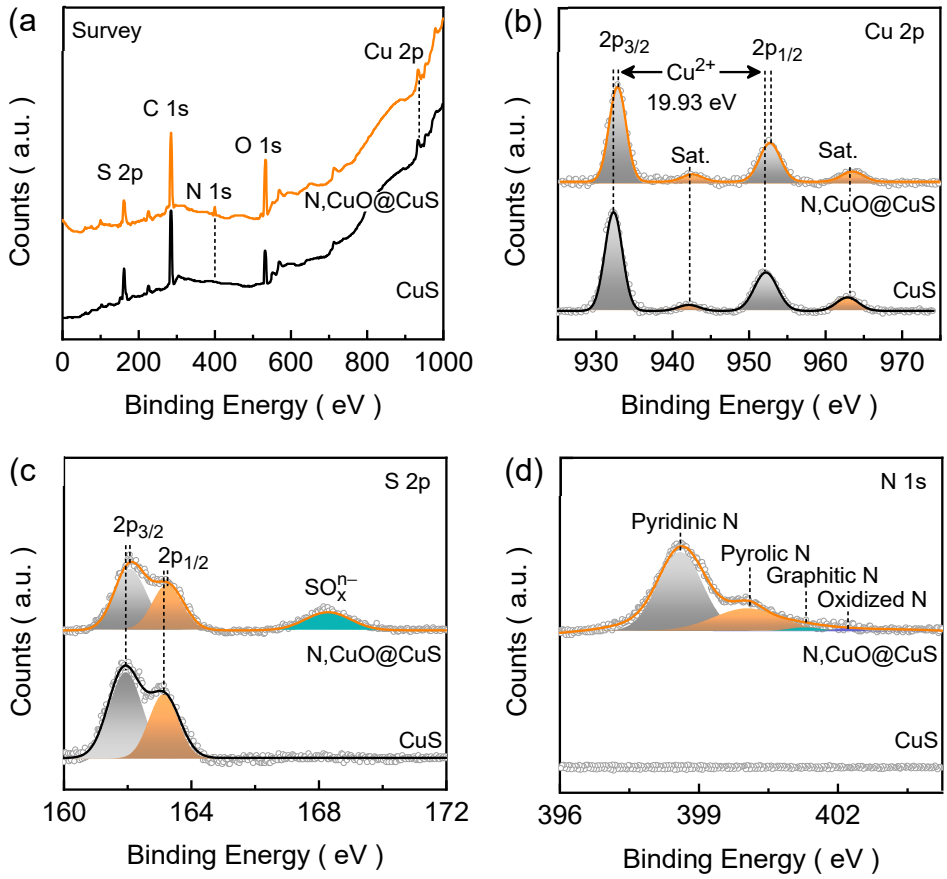

Figure 3. XPS (**a**) survey, (**b**) Cu 2p, (**c**) S 2p, and (**d**) N 1s spectra for CuS and N,CuO@CuS core-shell structure electrode films.

The narrow range S 2p spectra for CuS and N,CuO@CuS electrode films are shown in Figure 3c. The S 2p emission spectrum for CuS electrode film reveals two deconvoluted peaks related to S $2p_{3/2}$ (161.94 eV) and S $2p_{1/2}$ (163.13 eV) characteristic emissions [30]. The spin-energy separation of 1.19 eV for the characteristic sulfur emission confirms its S^{2-} state in the CuS structure [31]. The spin-energy of the distinctive S $2p_{3/2}$ and S $2p_{1/2}$ emissions are slightly right-shifted for the N,CuO@CuS electrode film, which affirms the successful bonding of N atom in the CuS lattice. Moreover, an additional wide peak appeared in the S 2p spectrum related to SO_x^{n-} (168.28 eV) emission and it could have originated due to the surface oxidation. The narrow range N 1s spectra for the CuS and N,CuO@CuS electrode films are presented in Figure 3d. Undoubtedly, the emission peaks appeared only for the CuO@CuS electrode film. These emission peaks are associated with pyridinic N (i.e., metal-nitrogen bonding, 398.60 eV), pyrrolic N (400.05 eV), graphitic N (401.31 eV), and oxidized N (402.23 eV), respectively [32,33]. The pyridinic and pyrrolic N species peaks contribute significantly to the spectrum and help to enhance the catalytic active sites and conductivity of the doped material. Nonetheless, the

Preprints (www.preprints.org) | NOT PEER-REVIEWED | Posted: 14 November 2023 doi:10.20944/preprints202311.0890.v1

oxidation states of Cu^{2+} and S^{2-} reconfirm the formation of CuS phase, and the presence of N and SO_x^{n-} species confirms the successful doping of N atom into the CuS lattice and the surface oxidation of the catalyst structure.

3.4. Electrochemical OER Performances

The JR-corrected LSV curves for the CuS and N,CuO@CuS electrodes are shown in Figure 4a. For comparison, the LSV curve for NF substrate was also recorded at the experimental conditions. Clearly, the catalytic of the NF substrate is relatively much poorer than those of the formed catalysts. The N,CuO@CuS electrode demonstrates good electrochemical activity by attaining the smaller overpotential of 240 mV at a driving current density of 10 mA cm^{-2}, whereas the pristine CuS catalyst attains only 268 mV at the similar current density. The change in overpotential is linked with boosted reaction kinetics, which can be understood by analyzing Tafel plots. Figure 4b shows the obtained Tafel plots from the LSV curves using the following equation:

$$\eta = [\log (J) \times b] + a, \quad (4)$$

where b and a are the Tafel slope and constant of the equation, respectively. The CuS and N,CuO@CuS catalyst demonstrates the Tafel slope of 194 and 138 mV dec^{-1}, respectively. The decrease in the Tafel slope value implies that the N,CuO@CuS catalyst has better electrochemical kinetics than to the pristine CuS catalyst. This is because incorporation of nitrogen facilitates catalytically active surface area (Figure S4) and material conductivity (Figure S1b), which results in improved rate of reaction kinetics, supported by turnover frequency analysis.

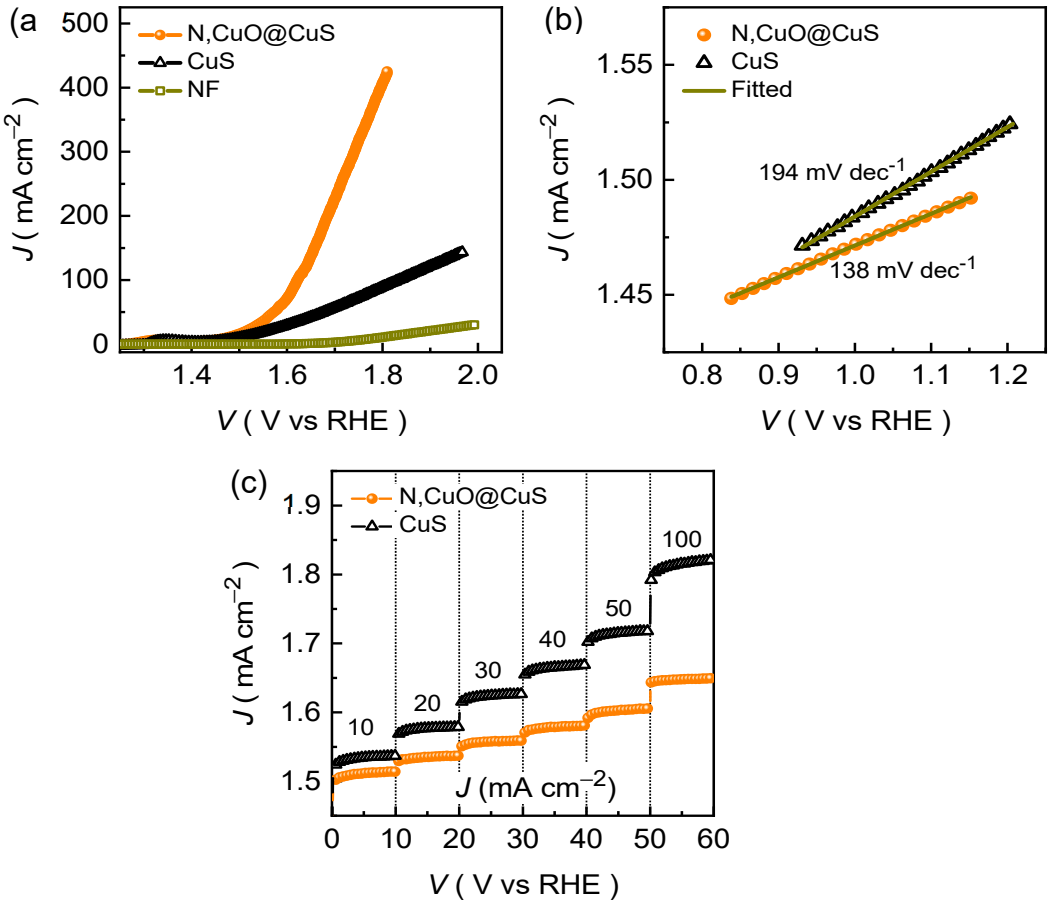

Figure 4. (**a**) LSV curves, (**b**) Tafel plots, and (**c**) voltage step profile for CuS and N,CuO@CuS core-shell structure electrode films.

Preprints (www.preprints.org) | NOT PEER-REVIEWED | Posted: 14 November 2023 doi:10.20944/preprints202311.0890.v1

The N,CuO@CuS catalyst demonstrates excellent electrochemical activity at a higher current density of 20, 30, 40, 50, and 100 mA cm^{-2} by achieving the small overpotential of 282, 307, 328, 341 and 392 mV, respectively. Moreover, the N,CuO@CuS catalyst exhibits the static potential response at various current rates while maintaining the smallest potential response at each driven current density, which is shown in the chronopotentiometric plots (Figure 4c). Besides, the superior endurance during the stability test is another crucial characteristic of the good OER catalyst electrode. Figure 5a demonstrates the long-tenure stability of the formed N,CuO@CuS catalyst that was recorded at different current rates in alkaline KOH conditions. The chronopotentiometric curve recorded at a current density of 10 mA cm^{-2} demonstrates a rapid increment in the potential during the initial testing might be due to an electrochemical activation (i.e., phase transformation), and then potential remains almost unaffected throughout the OER stability test. Moreover, the N,CuO@CuS catalyst exhibits excellent endurance during the long-time resilience at a higher current density of 50 and 100 mA cm^{-2}. Nonetheless, the post-stability measured almost identical EIS (Figure 5b) and LSV (Figure 5c) curves further attest the excellent long-term OER performance in alkaline medium.

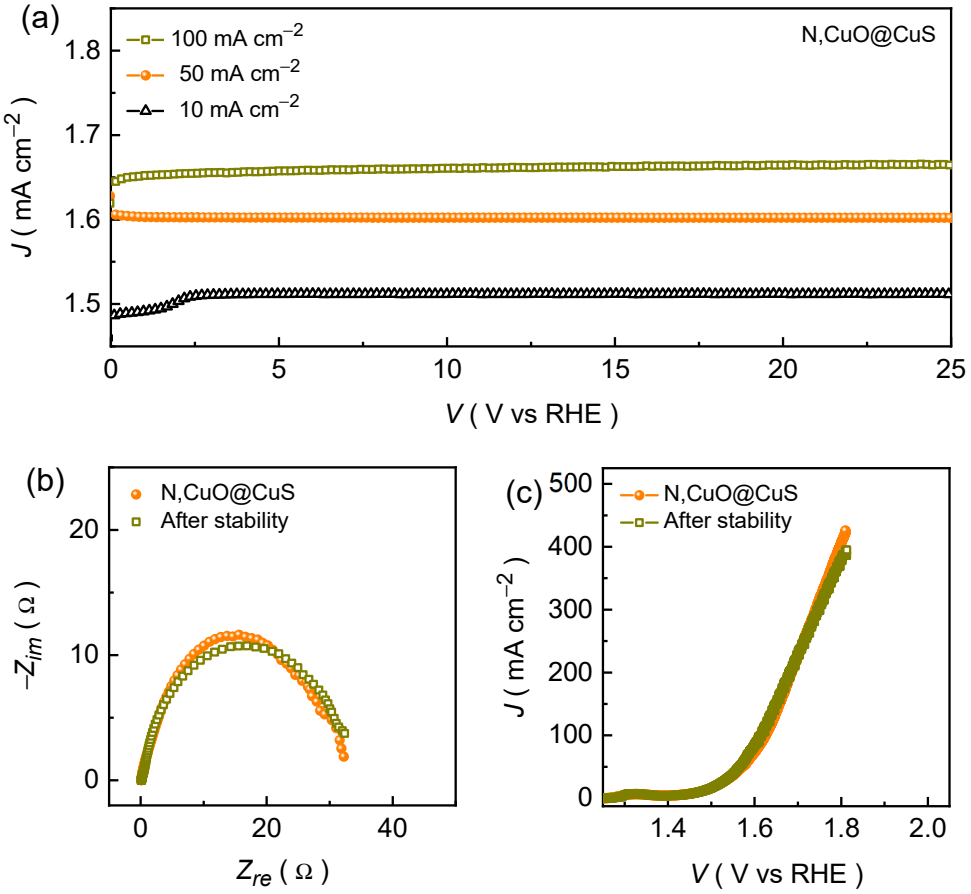

Figure 5. (**a**) Chronopotentiometric long-term stability, post-stability measured (**b**) Nyquist impedance plots, and (**c**) LSV curves for N,CuO@CuS core-shell structure electrode film.

5. Conclusions

The N,CuO@CuS core-shell structure was successfully synthesized on the 3D porous NF substrate via a mild hydrothermal procedure followed by nitrogenation process. The surface topography of the pristine CuS was completely altered after the nitrogen treatment and a flake-like textured shell appeared on the surface, which might be beneficial for protecting the formed core-shell structured catalyst from degradation during electrocatalytic OER stability. The N,CuO@CuS catalyst demonstrates excellent OER performance by achieving the small overpotential of 240 and 392 mV compared to the pristine CuS catalyst (268 and 602 mV) at 10 and 100 mA cm^{-2}, respectively, with a

modest Tafel slope of 138 mV dec^{-1}. In addition, the N,CuO@CuS catalyst exhibits excellent voltage-step profile with a static potential response at various current densities and reveals good endurance over 25 h chronopotentiometric stability testing at 10, 50, and 100 mA cm^{-2}. The excellent catalytic OER activity of the core-shell structure is a result of doped nitrogen atom, which alters the catalyst conductivity and catalytically active site and results in the boosted reaction kinetics favourable for electrochemical OER process.

Supplementary Materials: The following supporting information can be downloaded at the website of this paper posted on Preprints.org. Figure S1: OER performance reliability and Nyquist impedance curves; Figure S2: EDS image mapping; Figure S3: EDS spectra; Figure S4: non-Faradaic CV curves for the estimation ECSA.

Author Contributions: Investigation, methodology, visualization, and writing—original draft preparation, A.T.A.A.; Conceptualization, A.S.A.; validation, V.G.S.; software, A.J.; software, A.M.; data curation, S.S.; formal analysis, S.C.; project administration and funding acquisition, H.K.; resources, supervision, writing—review and editing, H.I. All authors have read and agreed to the published version of the manuscript.

Funding: This research was supported by the National Research Foundation of Korea through the Basic Science Research Program (Grant nos. 2021R1A2B5B01001796, 2021R1A2C1006113, and 2021R1A4A5031805).

Data Availability Statement: The data presented in this study are available on reasonable request from the corresponding author.

Conflicts of Interest: The authors declare no conflict of interest.

References

1. Zou, Z.; Ye, J.; Sayama, K.; Arakawa, H. Direct splitting of water under visible light irradiation with an oxide semiconductor photocatalyst. *Nature* **2001**, *414*, 625-627, doi:10.1038/414625a.
2. Lewis, N.S.; Nocera, D.G. Powering the planet: Chemical challenges in solar energy utilization. *Proceedings of the National Academy of Sciences* **2006**, *103*, 15729-15735, doi:doi:10.1073/pnas.0603395103.
3. Saeedmanesh, A.; Mac Kinnon, M.A.; Brouwer, J. Hydrogen is essential for sustainability. *Current Opinion in Electrochemistry* **2018**, *12*, 166-181, doi:https://doi.org/10.1016/j.coelec.2018.11.009.
4. Xu, D.; Stevens, M.B.; Cosby, M.R.; Oener, S.Z.; Smith, A.M.; Enman, L.J.; Ayers, K.E.; Capuano, C.B.; Renner, J.N.; Danilovic, N.; et al. Earth-Abundant Oxygen Electrocatalysts for Alkaline Anion-Exchange-Membrane Water Electrolysis: Effects of Catalyst Conductivity and Comparison with Performance in Three-Electrode Cells. *ACS Catalysis* **2019**, *9*, 7-15, doi:10.1021/acscatal.8b04001.
5. Park, S.; Shao, Y.; Liu, J.; Wang, Y. Oxygen electrocatalysts for water electrolyzers and reversible fuel cells: status and perspective. *Energy & Environmental Science* **2012**, *5*, 9331-9344, doi:10.1039/C2EE22554A.
6. Suen, N.-T.; Hung, S.-F.; Quan, Q.; Zhang, N.; Xu, Y.-J.; Chen, H.M. Electrocatalysis for the oxygen evolution reaction: recent development and future perspectives. *Chemical Society Reviews* **2017**, *46*, 337-365, doi:10.1039/C6CS00328A.
7. Aqueel Ahmed, A.T.; Hou, B.; Chavan, H.S.; Jo, Y.; Cho, S.; Kim, J.; Pawar, S.M.; Cha, S.; Inamdar, A.I.; Kim, H.; et al. Self-Assembled Nanostructured $CuCo_2O_4$ for Electrochemical Energy Storage and the Oxygen Evolution Reaction via Morphology Engineering. *Small* **2018**, *14*, 1800742, doi:https://doi.org/10.1002/smll.201800742.
8. Katsounaros, I.; Cherevko, S.; Zeradjanin, A.R.; Mayrhofer, K.J.J. Oxygen Electrochemistry as a Cornerstone for Sustainable Energy Conversion. *Angewandte Chemie Int. Edition* **2014**, *53*, 102-121, doi:https://doi.org/10.1002/anie.201306588.
9. Song, F.; Bai, L.; Moysiadou, A.; Lee, S.; Hu, C.; Liardet, L.; Hu, X. Transition Metal Oxides as Electrocatalysts for the Oxygen Evolution Reaction in Alkaline Solutions: An Application-Inspired Renaissance. *J. American Chem. Soc.* **2018**, *140*, 7748-7759, doi:10.1021/jacs.8b04546.
10. Roger, I.; Symes, M.D. First row transition metal catalysts for solar-driven water oxidation produced by electrodeposition. *J. Mater. Chem. A* **2016**, *4*, 6724-6741, doi:10.1039/C5TA09423B.
11. Pawar, S.M.; Pawar, B.S.; Babar, P.T.; Aqueel Ahmed, A.T.; Chavan, H.S.; Jo, Y.; Cho, S.; Kim, J.; Inamdar, A.I.; Kim, J.H.; et al. Electrosynthesis of copper phosphide thin films for efficient water oxidation. *Mater. Lett.* **2019**, *241*, 243-247, doi:https://doi.org/10.1016/j.matlet.2019.01.118.
12. Zhang, M.-T.; Chen, Z.; Kang, P.; Meyer, T.J. Electrocatalytic Water Oxidation with a Copper(II) Polypeptide Complex. *J. American Chem. Soc.* **2013**, *135*, 2048-2051, doi:10.1021/ja3097515.

13. Sagar, P.; Arun Kumar, N.S.; Shreenivasa, L.; Srinivasa, N.; De, D.; Yogeeshwari, R.T.; Siddaramanna, A. Citric acid assisted one-pot approach to synthesize CuO, CuO/Cu_2O, Cu/Cu_2O, and metallic Cu: potential electrocatalyst for enhanced OER. *Ionics* **2023**, *29*, 711-719, doi:10.1007/s11581-022-04851-6.
14. Ahmed, A.T.A.; Ansari, A.S.; Pawar, S.M.; Shong, B.; Kim, H.; Im, H. Anti–corrosive FeO decorated CuCo2S4 as an efficient and durable electrocatalyst for hydrogen evolution reaction. *Appl. Surface Science* **2021**, *539*, 148229, doi:https://doi.org/10.1016/j.apsusc.2020.148229.
15. Aqueel Ahmed, A.T.; Sekar, S.; Lee, S.; Im, H.; Preethi, V.; Ansari, A.S. Nitrogen-doped cobalt sulfide as an efficient electrocatalyst for hydrogen evolution reaction in alkaline and acidic media. *Int. J. Hydrogen Energy* **2022**, *47*, 40340-40348, doi:https://doi.org/10.1016/j.ijhydene.2022.04.076.
16. Deng, Y.H.; Tao, B.X.; Ye, C.; Zhang, Q.; Chen, G.; Wang, X.H.; Shi, Y.; Chen, J.R.; Luo, H.Q.; Li, N.B. N-doped cobalt disulfide decorated on carbon cloth as an efficient electrode for oxygen generation. *International Journal of Hydrogen Energy* **2019**, *44*, 16615-16623, doi:https://doi.org/10.1016/j.ijhydene.2019.04.160.
17. Kundu, J.; Khilari, S.; Bhunia, K.; Pradhan, D. Ni-Doped CuS as an efficient electrocatalyst for the oxygen evolution reaction. *Catalysis Science & Technology* **2019**, *9*, 406-417, doi:10.1039/C8CY02181C.
18. Li, Q.; Wang, X.; Tang, K.; Wang, M.; Wang, C.; Yan, C. Electronic Modulation of Electrocatalytically Active Center of Cu_7S_4 Nanodisks by Cobalt-Doping for Highly Efficient Oxygen Evolution Reaction. *ACS Nano* **2017**, *11*, 12230-12239, doi:10.1021/acsnano.7b05606.
19. Ahmed, A.T.A.; Pawar, S.M.; Inamdar, A.I.; Im, H.; Kim, H. Fabrication of FeO@$CuCo_2S_4$ multifunctional electrode for ultrahigh-capacity supercapacitors and efficient oxygen evolution reaction. *Int. J. Energy Research* **2020**, *44*, 1798-1811, doi:https://doi.org/10.1002/er.5027.
20. Zhu, J.; Zi, S.; Zhang, N.; Hu, Y.; An, L.; Xi, P. Surface Reconstruction of Covellite CuS Nanocrystals for Enhanced OER Catalytic Performance in Alkaline Solution. *Small* **2023**, *19*, 2301762, doi:https://doi.org/10.1002/smll.202301762.
21. Chakraborty, B.; Kalra, S.; Beltrán-Suito, R.; Das, C.; Hellmann, T.; Menezes, P.W.; Driess, M. A Low-Temperature Molecular Precursor Approach to Copper-Based Nano-Sized Digenite Mineral for Efficient Electrocatalytic Oxygen Evolution Reaction. *Chem. – An Asian J.* **2020**, *15*, 852-859, doi:https://doi.org/10.1002/asia.202000022.
22. Pawar, S.M.; Pawar, B.S.; Hou, B.; Kim, J.; Aqueel Ahmed, A.T.; Chavan, H.S.; Jo, Y.; Cho, S.; Inamdar, A.I.; Gunjakar, J.L.; et al. Self-assembled two-dimensional copper oxide nanosheet bundles as an efficient oxygen evolution reaction (OER) electrocatalyst for water splitting applications. *J. Mater. Chem. A* **2017**, *5*, 12747-12751, doi:10.1039/C7TA02835K.
23. Zhu, L.; Liu, L.; Huang, G.; Zhao, Q. Hydrogen evolution over N-doped CoS_2 nanosheets enhanced by superaerophobicity and electronic modulation. *Appl. Surface Science* **2020**, *504*, 144490, doi:https://doi.org/10.1016/j.apsusc.2019.144490.
24. Chaki, S.H.; Tailor, J.P.; Deshpande, M.P. Covellite CuS – Single crystal growth by chemical vapour transport (CVT) technique and characterization. *Mater. Science in Semiconductor Processing* **2014**, *27*, 577-585, doi:https://doi.org/10.1016/j.mssp.2014.07.038.
25. Rashad, M.; Rüsing, M.; Berth, G.; Lischka, K.; Pawlis, A. CuO and Co_3O_4 Nanoparticles: Synthesis, Characterizations, and Raman Spectroscopy. *J. Nanomaterials* **2013**, *2013*, 714853, doi:10.1155/2013/714853.
26. Deng, Y.; Handoko, A.D.; Du, Y.; Xi, S.; Yeo, B.S. In Situ Raman Spectroscopy of Copper and Copper Oxide Surfaces during Electrochemical Oxygen Evolution Reaction: Identification of CuIII Oxides as Catalytically Active Species. *ACS Catalysis* **2016**, *6*, 2473-2481, doi:10.1021/acscatal.6b00205.
27. Adhikari, S.; Sarkar, D.; Madras, G. Hierarchical Design of CuS Architectures for Visible Light Photocatalysis of 4-Chlorophenol. *ACS Omega* **2017**, *2*, 4009-4021, doi:10.1021/acsomega.7b00669.
28. Goswami, M.; Kumar, S.; Singh, N.; Sathish, N.; Ashiq, M.; Kumar, S. Effect of electrolyte cations on electrochemical performance of pseudocapacitive CuS electrode. *Ionics* **2021**, *27*, 5277-5285, doi:10.1007/s11581-021-04241-4.
29. Chen, P.; Zhou, T.; Chen, M.; Tong, Y.; Zhang, N.; Peng, X.; Chu, W.; Wu, X.; Wu, C.; Xie, Y. Enhanced Catalytic Activity in Nitrogen-Anion Modified Metallic Cobalt Disulfide Porous Nanowire Arrays for Hydrogen Evolution. *ACS Catalysis* **2017**, *7*, 7405-7411, doi:10.1021/acscatal.7b02218.
30. Jin, X.; Li, J.; Chen, G.; Xue, C.; Liu, W.; Zhu, C. Preparation of Cu_2ZnSnS_4-based thin film solar cells by a combustion method. *Solar Energy Materials and Solar Cells* **2016**, *146*, 16-24, doi:https://doi.org/10.1016/j.solmat.2015.11.027.

31. Sekar, S.; Brindha Devi, S.; Maruthasalamoorthy, S.; Maiyalagan, T.; Kim, D.Y.; Lee, S.; Navamathavan, R. One-step facile hydrothermal synthesis of rGO-CoS_2 nanocomposites for high performance HER electrocatalysts. *Int. J. Hydrogen Energy* **2022**, *47*, 40359-40367, doi:https://doi.org/10.1016/j.ijhydene.2022.04.069.
32. Fechler, N.; Fellinger, T.-P.; Antonietti, M. One-pot synthesis of nitrogen–sulfur-co-doped carbons with tunable composition using a simple isothiocyanate ionic liquid. *J. Mater. Chem. A* **2013**, *1*, 14097-14102, doi:10.1039/C3TA13435K.
33. Jiang, E.; Jiang, J.; Huang, G.; Pan, Z.; Chen, X.; Wang, G.; Ma, S.; Zhu, J.; Shen, P.K. Porous nanosheets of Cu_3P@N,P co-doped carbon hosted on copper foam as an efficient and ultrastable pH-universal hydrogen evolution electrocatalyst. *Sustainable Energy & Fuels* **2021**, *5*, 2451-2457, doi:10.1039/D1SE00161B.